

# Optical Engineering

[SPIDigitalLibrary.org/oe](http://SPIDigitalLibrary.org/oe)

## **Space Surveillance Telescope: focus and alignment of a three mirror telescope**

Deborah Freedman Woods  
Ronak Y. Shah  
Julie A. Johnson  
Alexander Szabo  
Eric C. Pearce  
Richard L. Lambour  
Walter J. Faccenda

# Space Surveillance Telescope: focus and alignment of a three mirror telescope

**Deborah Freedman Woods**

**Ronak Y. Shah**

MIT Lincoln Laboratory

244 Wood Street

Lexington, Massachusetts 02420

E-mail: [deborah.woods@ll.mit.edu](mailto:deborah.woods@ll.mit.edu)

**Julie A. Johnson**

**Alexander Szabo**

MIT Lincoln Laboratory

Stallion Range Center

Building 34560

Socorro, New Mexico 87801

**Eric C. Pearce**

**Richard L. Lambour**

**Walter J. Faccenda**

MIT Lincoln Laboratory

244 Wood Street

Lexington, Massachusetts 02420

**Abstract.** The Space Surveillance Telescope (SST) is a three-mirror Mersenne-Schmidt telescope with a 3.5 m primary mirror. It is designed to rapidly scan for space objects, particularly along the geosynchronous belt, approximately 36,000 km above the Earth. The SST has an unusually short focal ratio of F/1.0 and employs a camera composed of curved charge-coupled devices to match the telescope's inherent field curvature. The field-of-view of the system is 6 square degrees. While the unique system design is advantageous for space surveillance capabilities, it presents a challenge to alignment due to an inherently small depth of focus and the additional degrees of freedom introduced with a powered tertiary mirror. The alignment procedure developed for the SST at zenith pointing is discussed, as well as the maintenance of focus and alignment of the system across a range of elevation and temperature conditions. Quantitative performance metrics demonstrate the success of the system alignment during the telescope's first year of operation. © The Authors. Published by SPIE under a Creative Commons Attribution 3.0 Unported License. Distribution or reproduction of this work in whole or in part requires full attribution of the original publication, including its DOI. [DOI: [10.1117/1.OE.52.5.053604](https://doi.org/10.1117/1.OE.52.5.053604)]

Subject terms: telescopes; alignment; wavefront sensors; astronomy.

Paper 130113 received Jan. 22, 2013; revised manuscript received Apr. 12, 2013; accepted for publication Apr. 12, 2013; published online May 7, 2013.

## 1 Introduction

The Space Surveillance Telescope (SST), sponsored by the Defense Advanced Research Projects Agency (DARPA) is a 3.5 m diameter Mersenne-Schmidt telescope with a curved focal surface. The camera mosaic of 12 charge-coupled devices (CCDs) employs curved substrates built to the shape of the telescope's focal surface tiled across a 6 square degree field-of-view (FOV). The telescope has an extremely short focal ratio, F/1.0, whose compact layout ensures a highly agile pointing system. Figure 1 shows a model of the optical system. Table 1 lists the system parameters, including details of the CCD mosaic. The combination of wide FOV and pointing performance enables SST to rapidly scan the entire sky. Its location on an 8000-foot peak in the White Sands Missile Range (WSMR) south of Socorro, New Mexico, USA, provides a dry environment with excellent seeing conditions.

The SST's mission is to perform space surveillance and space situational awareness. That is, the telescope provides the position with respect to the stars and the brightness of satellites and space debris, particularly at the geosynchronous region located at approximately 36,000 km from the Earth's surface. MIT Lincoln Laboratory developed the program and L-3 Brashear built the telescope optics and mount. The telescope achieved first light in February 2011 and is currently transitioning from a commissioning to an operational phase.

While the unique design of the SST is advantageous for space surveillance, it creates a challenge to alignment as a result of the inherently small depth of focus and the additional degrees of freedom introduced with a powered tertiary mirror. Furthermore, the installation of the large CCD array at the prime focus of the telescope does not allow us to use a dedicated wavefront sensor or other special focusing

instrumentation. Instead, we align SST's optics using only intra- and extra-focal images of stars.

The alignment process for two mirror telescopes is well documented and demonstrated in operation.<sup>1-5</sup> The technique described by McLeod<sup>1</sup> for the case of a Ritchie-Cretien telescope is to first remove coma by a translation or tilt of the secondary mirror about its vertex. The coma produced by miscollimation does not vary across the FOV and so identifying and correcting for coma observed on-axis is sufficient for coma correction for the full field. However, the astigmatism produced by miscollimation varies as a function of field position. Alignment of the two mirror telescope is accomplished by observing the effects of astigmatism at multiple off-axis field positions and applying translation and tilt to the secondary mirror to remove the astigmatism due to miscollimation. Astigmatism that is intrinsic to the optical prescription will present a recognizable signature that can be separated from the astigmatism due to miscollimation.<sup>1</sup>

Theoretical expectations for alignment of three mirror telescopes have been described in recent literature. Thompson et al.<sup>6</sup> discuss the optical aberrations generated by misalignment of a three mirror anastigmatic (TMA) telescope, such as for the future James Webb Space Telescope. The misalignment-induced aberrations that will most significantly affect the image quality are coma and astigmatism. Thompson et al. note that while coma can be effectively canceled by a combination of mirror tilt and decenter, the resulting mirror positions will not generally remove astigmatism due to misalignment. The astigmatism must be measured at multiple field positions to be fully characterized. In addition, they describe a field-asymmetric aberration that is intrinsic to the TMA optical design. Characterization of this field-asymmetric aberration aids alignment. Plans for alignment of the three-mirror Large Synoptic Survey Telescope

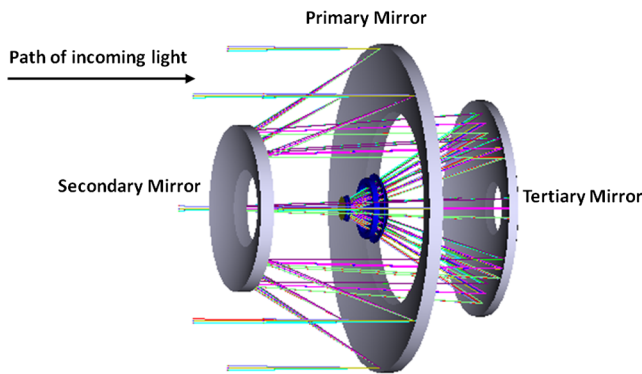


**Fig. 1** Optical layout of the SST. Light enters the system from the left in this image.

**Table 1** Space Surveillance Telescope system parameters, including the optical system and the camera.

Telescope	
Diameter (actual)	3.50 m
Diameter (effective)	2.90 m
Effective focal length	3.49 m
Nominal field-of-view	3 × 2 deg
Camera	
Sensors (thinned, backside illuminated)	2 K × 4 K CCD
Pixel size	15 μm 0.89 arcsec
Mosaic	6 × 2 chips
Effective size	12288 × 8192 pixels
Readout time	0.65 to 1.30 s
Exposure time	0.025 to 10 s
Filter	Open (0.4 to 1.0 μm)
Image rotator	None

(LSST) have been developed based on nodal aberration theory.<sup>7</sup> The LSST team describes a method to construct a sparse sampling measurement of alignment prior to installation of the camera, and comparison of the measured aberrations with predicted sensitivities to misalignment. Their approach to alignment utilizes the nodal behavior of astigmatism to characterize mirror positioning. The LSST design, like that of a TMA or RC Cassegrain, presents bimodal astigmatism as the dominant misalignment induced aberration once 3rd order coma is corrected. Additional discussion of aberrations and alignment for a telescope with an arbitrary number of mirrors can be found in Ref. 8.

The SST is the first (to our knowledge) large three mirror telescope to achieve alignment in practice. The methods

employed at the SST to align the telescope at zenith pointing are similar in spirit to the techniques described for two and three mirror telescopes. We obtain a quantitative measure of the magnitude and direction of optical aberrations manifest in the system wavefront using defocused image techniques. The algorithms of the DONUT program, which we adapt for use with the SST, generate a measurement of optical aberrations from a single defocused star.<sup>9</sup> Comparison of the DONUT measured aberrations with the sensitivity analysis generated by a Zemax model of the as-built optical system leads to predictions for the required adjustments to mirror alignment. We accomplish the focus and alignment of the SST using a five-step iterative process to find the optimal mirror positions at a given temperature for the zenith pointing case.

After achieving optimal focus and alignment at zenith pointing, we then develop an elevation dependent focus and alignment model to correct for gravity sag. The elevation dependent corrections are applied real-time to maintain focus and alignment across all elevation angles. We likewise develop a model to describe the temperature dependent focus corrections. Real-time adjustments to focus as a function of mount structure temperature ensure that the system remains in focus as the temperature environment varies over the course of the night.

In this paper we describe the method that we developed for the focus and alignment of the SST and present quantitative measures of the alignment performance. Section 2 contains an introduction to the measurement and representation of wavefront aberrations; Sec. 3 describes the Zemax sensitivity analysis; Sec. 4 provides details on the focus and alignment method to achieve best focus at zenith pointing, including adjustments for different elevation angles in Sec. 4.1 and for temperature in Sec. 4.2. Section 5 provides performance results and Sec. 6 discusses applicability to other systems. We conclude in Sec. 7.

## 2 Measurement and Representation of Wavefront Aberrations

The telescope mirror alignment is accomplished through the measurement of optical aberrations present in the system. The shape of the wavefront produced by an optical system,  $W(\rho, \theta)$ , carries with it information on the optical aberrations of the system that generated it. A perfectly unaberrated wavefront is flat, as all rays traced through the optical system arrive at the exit pupil with zero path length differences. Aberrations can be described as path length differences resulting in deviations from flatness of the wavefront. For example, defocus is a radially symmetric aberration that increases with the square of the radial distance.

The Zernike polynomials provide a convenient representation of wavefront aberrations in an optical system because they form a complete basis that is orthogonal over the unit circle and have separable radial and angular contributions.<sup>10</sup> The Zernike terms relate directly to the familiar low order aberrations, including tilt, defocus, coma, astigmatism, and spherical aberration.<sup>11</sup> Figure 2 shows the wavefront aberrations in terms of the Zernike polynomials. The wavefront in terms of Zernike polynomials is defined as

$$W(\rho, \theta) = \sum_{n=0}^{\infty} \sum_{m=0}^n z_{nm} N_n^m P_n^m,$$

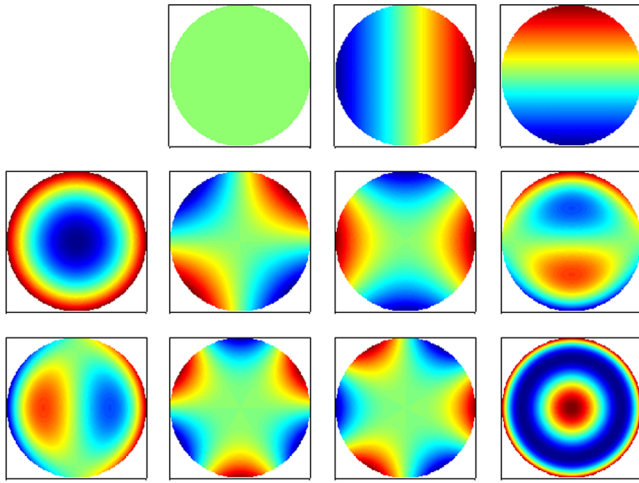


**Fig. 2** Zernike polynomial representation of an aberrated wavefront. The Zernike numbering system follows the Noll convention.<sup>12</sup>

where  $z_{nm}$  is the coefficient of best fit to the Zernike polynomial term. The Zernike coefficient tells the amount of associated optical aberration present in the optical system. A normalization factor,  $N_n^m$ , is used to make the set of Zernike polynomials orthonormal.

$$N_n^m = \sqrt{\frac{2(n+1)}{(1+\delta_{m0})}}$$

The Zernike polynomials are separated into radial and spatial contributions. The polynomials are numbered  $n$ ,  $m$ , which are the order of the radial and angular terms respectively. A single order  $p$  is sometimes used to describe a set of  $(n, m)$ , where for example  $z_{20} = Z4$  (defocus). Note that this paper uses the standard Noll convention for the ordering of the polynomials.<sup>12</sup> The polynomials are defined as follows:

$$\begin{aligned} P_n^m(\rho, \psi) &= R_n^m(\rho) \cos(m\psi) \\ P_n^{-m}(\rho, \psi) &= R_n^m(\rho) \sin(m\psi) \\ R_n^m(\rho) &= \sum_{k=0}^{\frac{n-m}{2}} \frac{(-1)^k (n-k)!}{k! \left(\frac{n+m}{2} - k\right)! \left(\frac{n-m}{2} - k\right)!} \rho^{n-2k}, \quad \text{for } n-m \text{ even} \\ R_n^m(\rho) &= 0, \quad \text{for } n-m \text{ odd.} \end{aligned}$$

The DONUT algorithm developed by Tokovinin and Heathcote<sup>9</sup> estimates the wavefront error in terms of the Zernike polynomials from the image of a single defocused star. The method is based on the relationship between the intensity distribution in a defocused image and the local wavefront curvature, which is described by the irradiance transport equation.<sup>13</sup> The DONUT method differs from phase diversity wavefront sensing,<sup>14</sup> the latter of which extracts a measurement of optical aberration from two images with a well characterized difference in aberration such as defocus. The technique of curvature sensing extracts a measure of optical aberration using two images with equal and opposite defocus aberration,<sup>15</sup> preferably observed simultaneously to avoid confusion from seeing induced aberrations.

DONUT generates an estimate of the wavefront aberrations by directly fitting a model of the aberrated image to the observed defocused star (which is donut shaped in the case of a telescope with a central obscuration, hence the name). An iterative fitting algorithm creates a model of the aberrated image and compares it with the observed image, which is successively refined until the model passes a  $\chi^2$  goodness-of-fit test in comparison with the observed image. The modeled image is generated as the sum of the Zernike polynomial terms; the magnitude and sign of the Zernike coefficients describe the form of the aberrated wavefront with appropriate contributions from the different terms. We adapt the DONUT code for use with the SST. We translate the code from Interactive Data Language (IDL) to MATLAB and develop automated processes for star-selection and image cut-outs to enable batch processing on 40+ stars per frame.

The contribution of each optical aberration to the total image blur is assessed from the Zernike terms measured for a set of stars in a given frame. Image blur is calculated from the Zernike polynomial derivative.<sup>16</sup> The Zernike polynomial derivative is directly proportional to the wavefront slope error, a relationship that is exploited by a Shack-Hartmann wavefront sensor. A Shack-Hartmann wavefront sensor uses the displacement of subaperture spots to compute the wavefront slope error, which is a direct measure of the coefficients of the Zernike polynomial derivatives. In the case of the SST, the DONUT algorithms compute the Zernike polynomial coefficients. Taking the derivative of the polynomials and applying the associated coefficients allows us to assess the wavefront slope error at each point on the wavefront. The displacement between the position of the theoretical subaperture spot that would be produced at each point on the aberrated wavefront and the position of the subaperture spot produced by the unaberrated case shows the effect of the aberration on the resulting image quality.

The image blur is defined as the root-mean-square (rms) of the displacements introduced across the wavefront by the aberrated system. It is useful to assess the contribution of each Zernike term to the total image blur for the set of all stars measured in a given frame; the relative contribution to total image blur for each aberration guides the decision of which aberrations are most important to correct. The relative importance of each aberration to the overall image quality is difficult to assess directly from the magnitude of the Zernike coefficients because of the variation in radial and angular orders of the different terms. Figure 3 shows an example set of subaperture spot displacements in a stellar image for the cases of defocus, astigmatism, coma, and trefoil.

### 3 Zemax Sensitivity Analysis

We control the bulk position of the mirrors in order to reduce aberrations: no surface bending or corrections are performed. The degrees of freedom that are available for focus and alignment are translation along the optical axis (piston), tip, tilt, and y-decenter for the tertiary and secondary mirrors. We constructed a sensitivity matrix based on these degrees of freedom using a Zemax model of the as-built telescope in order to determine mirror adjustments.

In some cases a given mirror motion, e.g., tilt of the tertiary mirror, may be predicted to improve a subset of

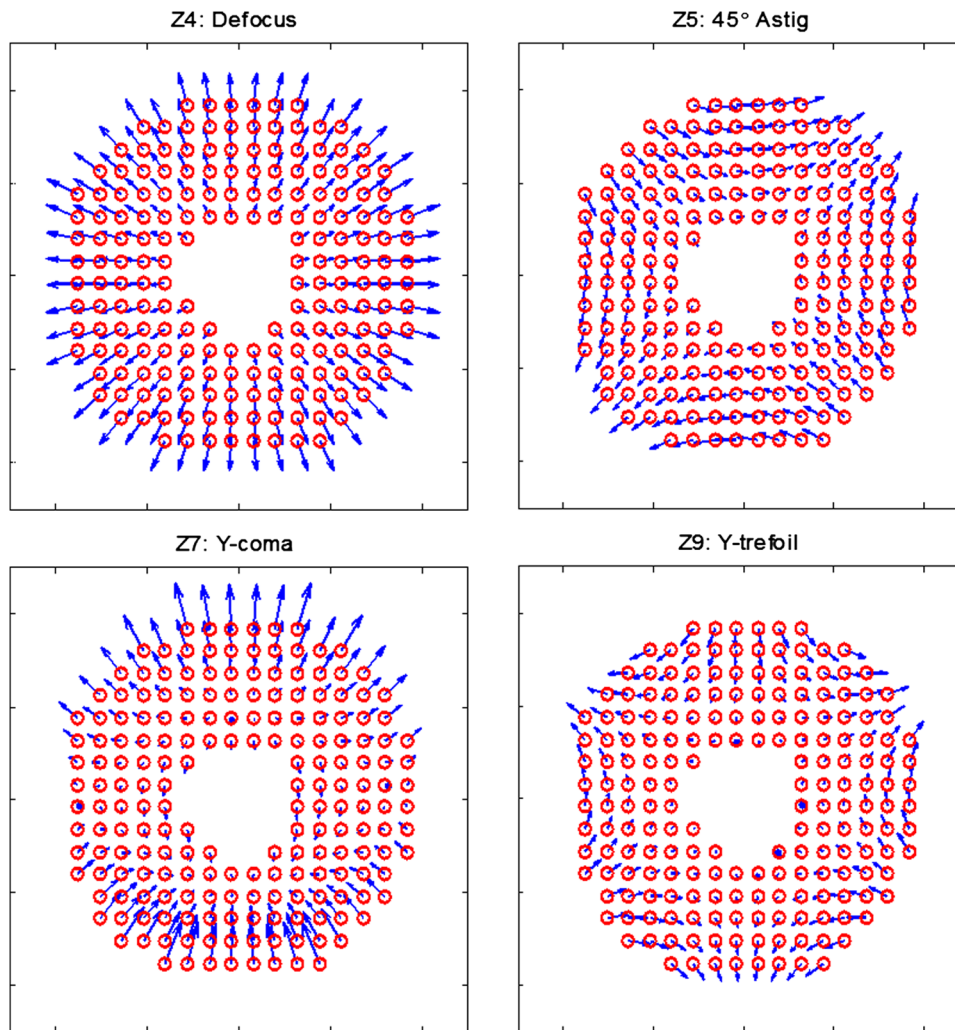


**Fig. 3** The contribution to image blur of each aberration is assessed from the rms of the subaperture spot displacements at each point on the wavefront. The figure on the top left shows the effect of Z4 (defocus): a radially symmetric shift outward in the subaperture spot position. The figure on the top right shows Z5 (astigmatism at  $45^\circ$ ). In the bottom row, the figure on the left shows Z7 (y-coma) and the figure on the right shows Z9 (y-trefoil). The amount of astigmatism, coma, etc. that is displayed in each figure is selected for the purpose of illustration, and do not represent the magnitude of aberrations present in an actual system.

the measured aberrations while worsening others. Ideally, a multiparameter optimization solution would predict the combination of mirror motions that would result in the best outcome. However, we found in practice that the uncertainty on the measurement of the higher order aberrations and the sensitivity of those aberrations to tiny shifts in mirror position made a simultaneous multiparameter approach impractical. Instead, we worked to reduce one aberration at a time by the appropriate mirror motion. This approach is practical because the effects of  $x$ -tilts or  $y$ -tilts (and similarly for decenters) are separable and linearly additive to first order. Figure 4 shows the Z7 or Z8 terms (y-coma or  $x$ -coma, respectively) predicted by the Zemax model as a function of mirror position for each of four cases of mirror motions. Note the terminology: SM = secondary mirror, TM = tertiary mirror.

Using this approach, we constructed the sensitivity matrix by varying one of the degrees of freedom at a time in Zemax, using step sizes that are about 2% of the available range. For example, the tertiary mirror piston travel range is  $\pm 1250 \mu\text{m}$ ; we used step sizes of  $25 \mu\text{m}$ . This was based on both Zemax comparisons of the resultant spot size

changes for such changes, the computational efficiency available to us at the time we produced the matrix values, and heuristic knowledge of the changes in spot size for the real system. A significantly larger step size would poorly sample the fit space available to us from our Zernike analysis, while smaller steps would produce an inefficient analysis. Figure 5 illustrates the Zemax modeled predictions of the point spread function (PSF) for the example cases of astigmatism and spherical aberration.

#### 4 Focus and Alignment Procedure

The method for focus and alignment of the SST at zenith is a five-step iterative process.<sup>17</sup> The preliminary spot size of the SST at first light, February 2011, measured  $70 \mu\text{m}$ . Initial efforts at coarse focus and alignment, including bulk alignment and shimming of the telescope mirror cells and the camera/corrector lens assembly, reduced the spot size to  $45 \mu\text{m}$ . Further reduction in spot size was accomplished with the iterative process described below, which was carried out over the course of several different nights during the first year of operation:

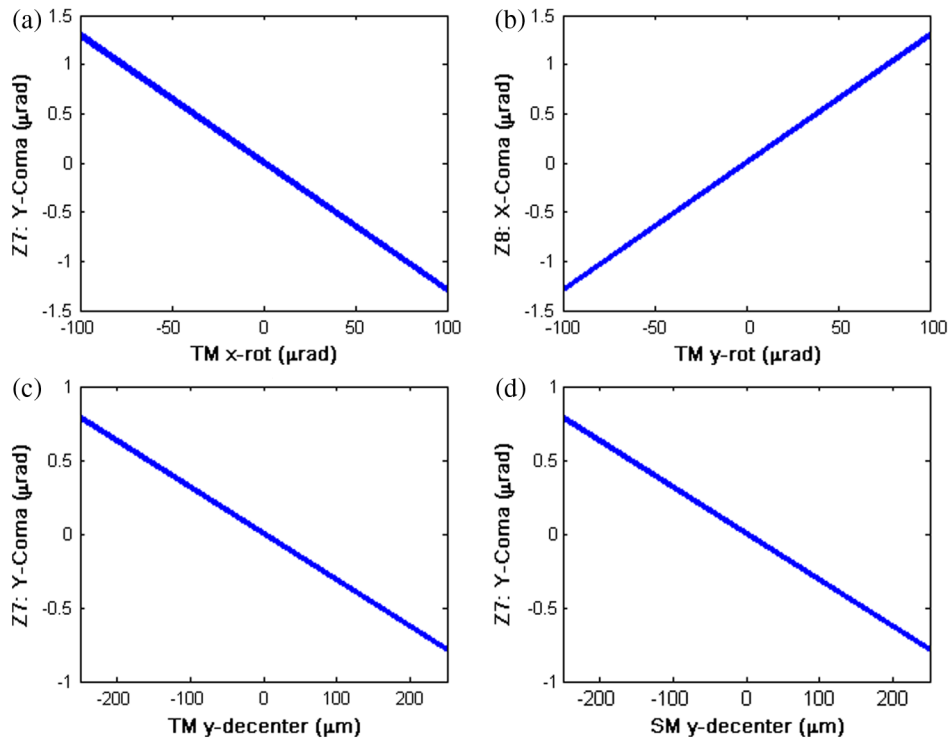
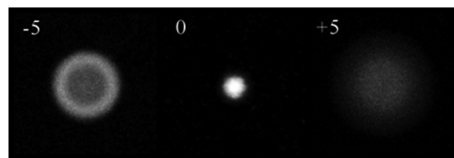


**Fig. 4** Zemax sensitivity analysis predictions for Z7 and Z8 terms (y-coma and x-coma, respectively) for x-rotation of the tertiary mirror (a), y-rotation of the tertiary mirror (TM, b), y-decenter of the tertiary mirror (TM, c) and y-decenter of the secondary mirror (TM, d).

1. Move the tertiary in piston to reduce defocus
2. reduce spherical aberration with tandem piston of secondary and tertiary mirrors
3. measure higher order aberrations
4. associate higher order aberrations with predictions of Zemax sensitivity matrix
5. apply mirror corrections and iterate steps 1-5 as needed.



Spherical Aberration



Astigmatism

**Fig. 5** The top panel shows the Zemax prediction for PSF with spherical aberration for in-focus and out-of-focus images. The bottom panel shows the Zemax prediction for misalignment induced astigmatism across the focal plane.

We repeat steps 1 through 5 to drive down the telescope spot size. The iterations continue until the spot size meets the system requirement. It is necessary to work on a night with excellent seeing conditions (subarcsec) and a stable temperature load on the telescope structure.

The first step of the alignment process is the familiar translation of the tertiary mirror along the optical axis to minimize defocus. We reduce focus by measuring the spot size for a series of tertiary mirror piston positions and fitting a quadratic to the curve of spot size as a function of mirror position. The minimum of the curve is the best focus position. In Fig. 6, the image compilation illustrates the variation in spot size achieved by stepping through tertiary mirror position. This step takes about five minutes for the automated focusing sequence to complete.

The second step removes spherical aberration. During our early analysis, we found that in-focus PSF values were larger than the expected system performance, although the

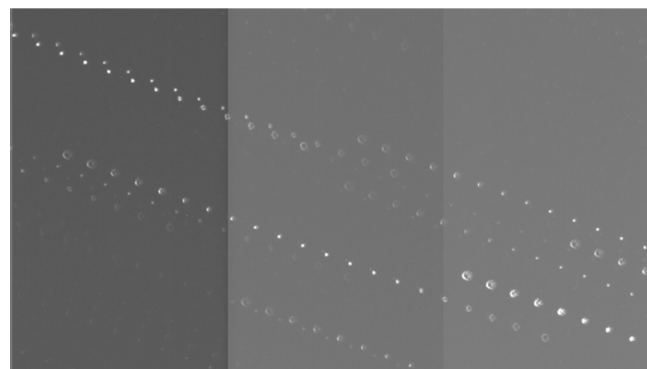


**Fig. 6** Actual data showing steps through tertiary mirror y (along the optical axis) to find the minimum spot size on average across the field.

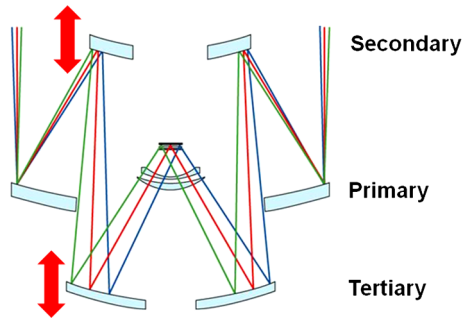


**Fig. 7** The coordinated translation of secondary and tertiary mirrors along the optical axis is necessary for removing spherical aberration.

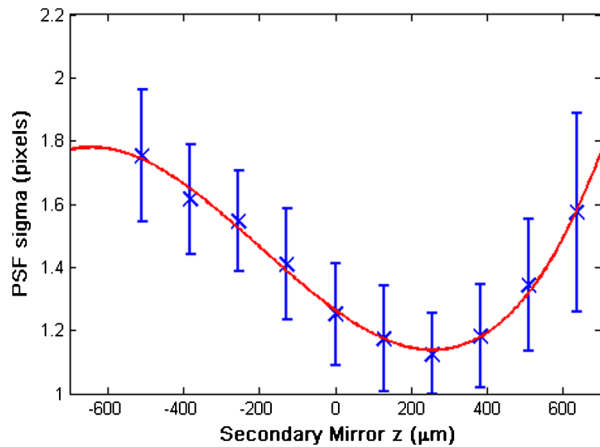


**Fig. 8** In-focus PSF size measured on actual data for coordinated moves of tertiary and secondary mirrors along the optical axis. The total path length remains constant, i.e., defocus aberration is unchanged while the spot size changes due to spherical aberration.

individual spots and the bulk pattern across the focal plane exhibited radial symmetry. We suspected that spherical aberration, which is radially symmetric across a focal surface just like defocus, was the likely contributor. It is tricky to measure spherical aberration using the DONUT algorithms because a purposely defocused system (tertiary mirror translated along the optical axis) also naturally induces spherical

aberration. Since the DONUT program is only used on defocused images, confusion exists when separating the contribution of spherical aberration due to the defocus step from what would be present in an in-focus image.

To reduce the spherical aberration in the system, we need to find the ideal mirror positions where both defocus and spherical aberration are simultaneously minimized. Analysis of the spherical aberration from the sensitivity matrix reveals that it grows with coordinated displacement of the tertiary and secondary pistons. Figure 7 illustrates the coordinated motion of secondary and tertiary piston that can be applied while maintaining a constant path length, i.e., constant defocus. The procedure for simultaneously minimizing both spherical aberration and defocus is to take the previously determined tertiary position that reduced defocus and perform a tandem piston with secondary mirror position. In Fig. 8, we see the variation in spot size that is produced by a coordinated motion of the tertiary and secondary mirrors. Focus is maintained (i.e., defocus is minimized) at every point, while the spot size changes due to the presence of spherical aberration. Figure 9 shows the DONUT measurement of Z11 (spherical aberration) present before (a) and after (b) finding the optimal combined tertiary and secondary mirror positions. This feature is unique to three mirror telescopes. We again measure the spot size for each tandem step and fit a quadratic. The minimum of the quadratic represents the best combined position of both mirrors. Step two also takes about 5 min for an automated sequence of mirror steps and spot size measurements to run.

The third step uncovers coma and astigmatism using out-of-focus star images; in this case, recall that the in-focus positions were determined using the previous two steps. The DONUT software is used to estimate the Zernike aberrations in the system as described in Sec. 2. Figure 10 illustrates the image data and the Zernike reconstruction of a single defocused star. We acquire images on either side of focus for comparison and estimates of systematic errors (weather, hydraulic control, etc.). The time for our algorithms to identify candidate stars for measurement and to run the DONUT software on approximately 40 stars per image takes about 10 min of processing time on a Linux machine with a 2.80 GHz processor.

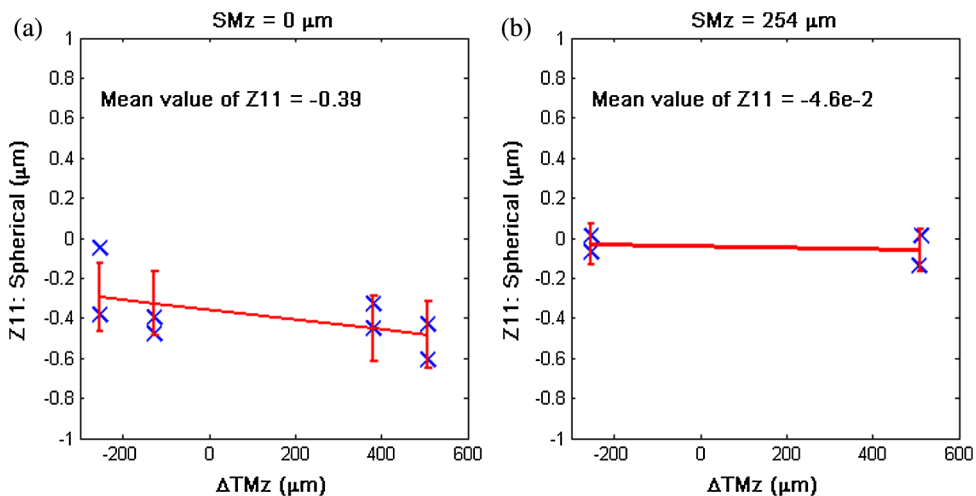


**Fig. 9** Average spherical aberration measured across the focal plane as a function of tertiary mirror piston for two different locations of the secondary mirror piston for actual data. The spherical aberration is reduced in the case shown in the left panel for a particular secondary mirror position.

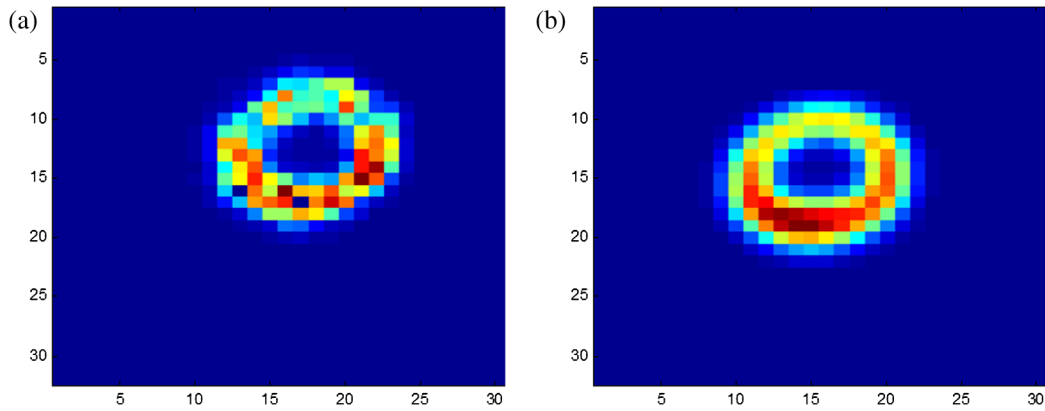


Fig. 10 (a) Image data and (b) Zernike reconstruction.

The fourth step is to consult the Zemax sensitivity analysis for association of the Zernike aberration coefficients measured by DONUT with predictions for compensatory mirror motions. In the fifth step, we apply the mirror alignment corrections, paying particular attention to coma and astigmatism, which are indicative of mirror tilts and offsets. It is necessary to repeat the measurements of defocus (step 1) and spherical aberration (step 2) after new mirror tilts are applied because the tilt also results in a change in the focus position for spots across the FOV. Analyzing the Zernike coefficient measurements and deciding on a course of action based on the Zemax sensitivity matrix includes some human oversight. The time for completion of this step varies with the complexity of the aberration profile and is carried out in the manner described at the beginning of Sec. 3.

#### 4.1 Maintaining Focus and Alignment under Gravity Sag

Once the mirror alignment at zenith pointing reaches performance goals, the next step is to measure the aberrations introduced as a function of elevation angle. Gravity causes the mirror position to sag as SST points away from zenith. The shape of the mirror itself is prevented from “potato-chipping” using a zero-force hydraulic return force on several 10’s to 100’s of actuators. Remaining misalignment of the bulk position is addressed by repeating the described process for multiple elevation steps.

We first measure the defocus as a function of elevation angle by stepping the tertiary mirror position along the optical axis to find the minimum spot size, as described in the previous section, at several elevation conditions. We find the defocus is well described by a quadratic line fit to the shift in tertiary mirror position as a function of elevation angle. After applying the correction to the tertiary fit, we then acquire a set of purposely defocused images for analysis with the DONUT program.

The most significant aberrations that appear as a function of elevation angle are the Z6 term (0-astigmatism) and Z7 term (y-coma) (cf. Fig. 11). There are a number of potential mirror motions that could be used to compensate for these aberrations. Tilt about the  $x$ -axis or translation along the  $y$ -axis of either the tertiary or secondary mirror introduce  $y$ -coma. The selection of which mirror motion model to apply was determined by consideration of other aberrations introduced into the system by the corrective mirror motions. We find the best results for overall aberration reduction and improved symmetry across the focal plane result from adjustment to the  $x$ -rotation of the tertiary mirror as a function of elevation angle. Figure 12 shows performance of the elevation correction in terms of the median spot size at each elevation, the spot size limits within which the upper 90% and lower 10% of all image frames at each elevation observed. The measured PSF value (rms diameter in units of  $\mu\text{m}$ ) is reported, along with the PSF corrected for elevation angle.

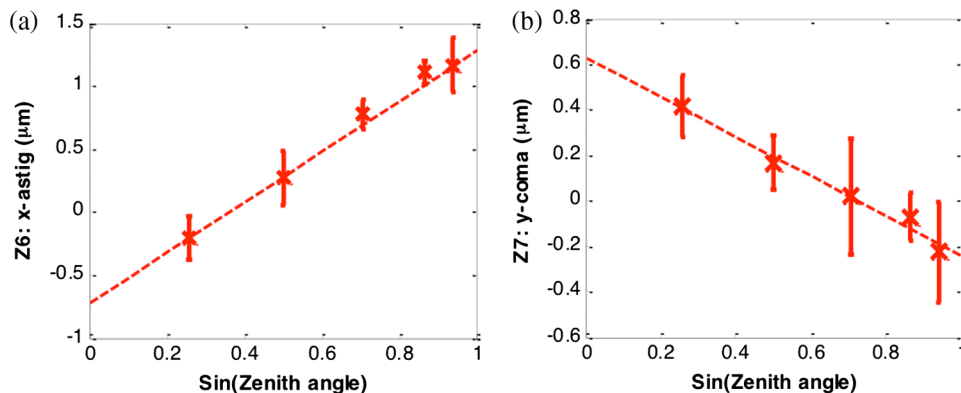
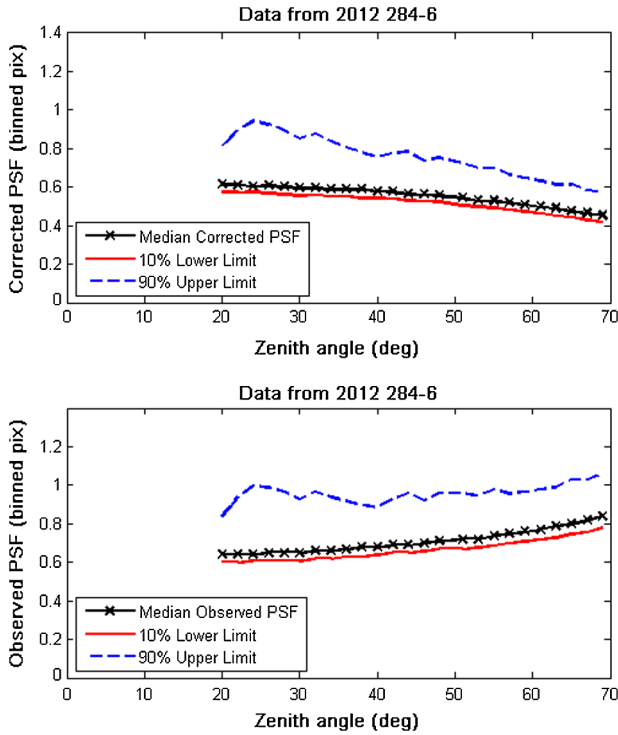


Fig. 11 (a) The measured Z6 term and (b) measured Z7 term show clear trends as a function of the zenith angle.



**Fig. 12** The performance of the elevation correction is demonstrated in the plot of spot size as a function of zenith angle for all observations on the typical nights of 2012 days 284 to 286. The upper panel shows the PSF after applying the correction for airmass, and the lower panel shows the observed (uncorrected) values. The atmospheric correction assumes the standard model where the PSF increases proportional to (airmass)<sup>0.6</sup>. The slight decrease in spot size at low elevation (large zenith angle) is due to a combination of improved alignment performance at low elevation and overestimation of the atmospheric correction on a night with good seeing conditions. The PSF is reported as rms diameter in units of  $\mu\text{m}$ .

#### 4.2 Maintaining Focus and Alignment across Temperature Variation

The steel telescope structure expands or contracts according to the ambient temperature. Over the course of a year, the nautical twilight temperature varies from a low of about  $-13^{\circ}\text{C}$  in winter to a high of  $25^{\circ}\text{C}$  in summer. Environmental control of the telescope dome, designed by M3 Engineering, helps to regulate the temperature environment. Dome preconditioning is used to minimize the temperature variation of the structure once operations begin. Even with these efforts, the structure temperature can still be expected to vary during the night.

We track the effect of temperature on the focus position with regular focus measurements in the manner described in step 1 of Sec. 4. Over the course of the first year of operation, we build a temperature model for the SST:

$$\text{TM}_z - \text{SM}_z = C_1 * T_{\text{avg}} + C_2,$$

where  $\text{TM}_z$  and  $\text{SM}_z$  are the tertiary mirror and secondary mirror position along the optical axis, respectively. The average temperature of the telescope structure is  $T_{\text{avg}}$ , and the linear coefficients of best fit are  $C_1 = 1.81$  and  $C_2 = 6.01$ . In practice, we adjust  $\text{TM}_z$  to focus the telescope, i.e., to minimize the defocus aberration. The location of  $\text{SM}_z$

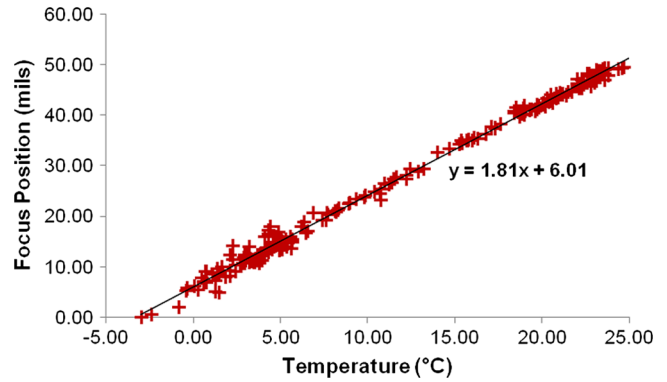


**Fig. 13** Empirical relationship between mirror positions along the optical axis (Tertiary Mirror  $z$ —Secondary Mirror  $z$ ) and average temperature of the telescope structure.

is selected to minimize spherical aberration as described in step 2 of Sec. 4, and its position also varies with the telescope structure temperature. We find that the model predicts the focus position to within  $25 \mu\text{m}$  of travel of the tertiary mirror at each temperature point when the system is in thermal equilibrium. Figure 13 shows the measured best focus position as a function of average temperature of the telescope structure.

The empirical model between mirror position and temperature uses the average of the 58 temperature sensors on the telescope structure. In theory, the mirror position should be most sensitive to the temperature of the struts supporting the mirror cells, which determines the thermal expansion of the component associated with the mirror placement along the optical axis. We experimented with using the sensors on the mirror struts to build a temperature model, but found that the resulting line fit was adversely affected by the noisier temperature measurement that was obtained using fewer sensors. Taking the average over all temperature sensors on the structure reduces the uncertainty in the temperature reading, an advantage that outweighs the benefit of using more targeted locations of the temperature probes.

### 5 Performance Results

The overall system performance of the SST depends strongly on its ability to maintain optimal focus during observations at all temperatures and elevation. An increased spot size would spread the target signal over additional pixels, decreasing the signal-to-noise ratio and degrading the limiting magnitude achieved by the system for a given set of observing conditions. System models predict the relationship between the increase in spot size and the change in limiting magnitude (Fig. 14).

A typical data set from 2012 days 284 to 286 reveals our overall performance across all elevation and temperatures throughout the nights' observing. Figure 15 shows the cumulative histogram of PSF values (after correcting for airmass) for all images observed in the data set. The median PSF value at all elevations after correcting for airmass is  $33 \mu\text{m}$  rms diameter, and the observed median PSF without airmass correction is  $43 \mu\text{m}$  rms diameter. We maintain nightly focus and alignment performance versus temperature and elevation to remain within  $<0.64$  magnitudes performance impact (after correcting for airmass) for 90% of the time.

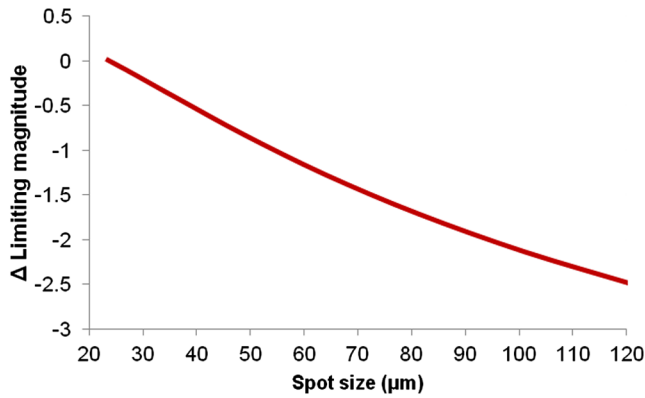


**Fig. 14** The predicted impact of spot size on the system performance in terms of limiting magnitude for a constant integration time and set of atmospheric conditions. The limiting magnitude degrades substantially as the spot size grows, smearing the signal over additional pixels and decreasing the signal-to-noise ratio.

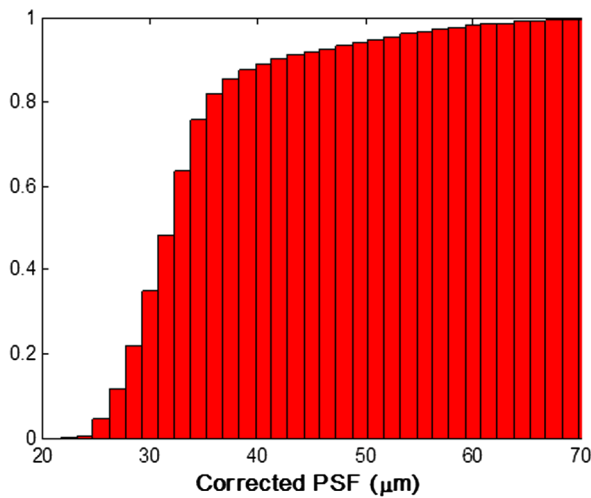


**Fig. 15** Cumulative histogram of PSF size (rms diameter in units of  $\mu\text{m}$ ). The data set is comprised of the average PSF in each images observed on 2012 days 284 to 286. The median corrected PSF value after correcting for airmass is  $33 \mu\text{m}$ , which corresponds to 0.3 magnitudes off optimal performance. The system maintains a PSF less than  $42 \mu\text{m}$  for 90% of the time, which corresponds to 0.6 magnitudes off optimal expectations (which is set for good seeing conditions.)

The pattern of spot size increase across the focal plane demonstrates the success of the alignment program in balancing the competing interests across the wide field-of-view. Figure 16 shows a map of the normalized spot diameter as a function of field position. The general pattern reveals the smallest spot size at the center and a gradual increase moving outward in all directions. The chips shown in the upper left and lower left corners fail to match this pattern, which we postulate is due to the alignment of the chips relative to the focal surface and relative to the other chips in the array. Despite the chip installation, the alignment of the system as a whole succeeds in creating an optimal pattern of spot size distribution across the six degree field-of-view. The impact on the realized magnitude limit of observations due to the spot size variation across the focal plane is illustrated in Fig. 17.

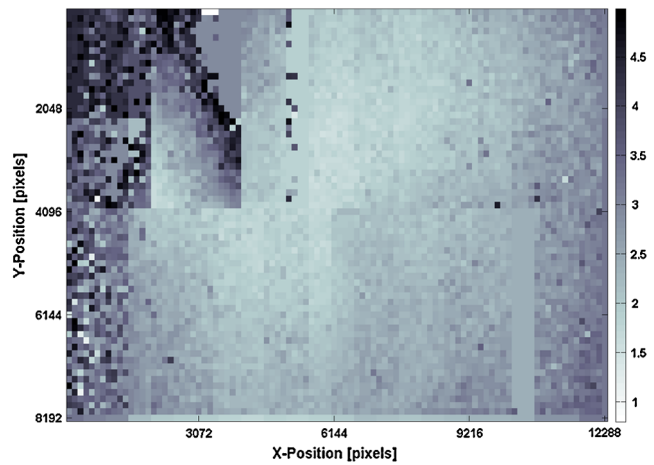


**Fig. 16** Map of normalized spot size across the focal plane. The data points show the mean spot size in  $128 \times 128$  pixels averaged over five frames of stellar imagery. The pixel gray scale is in units of relative PSF. The two chips in the upper left corner exhibit significantly degraded spot sizes compared with the remainder of the focal plane. Current hypothesis suggests that the performance impact is caused by the chip alignment relative to the focal plane, which explains the discontinuity observed around pixel coordinate  $x = 2000$  and  $4000$ . The remainder of the focal plane displays the expected radial symmetry that is consistent with optimal mirror alignment.

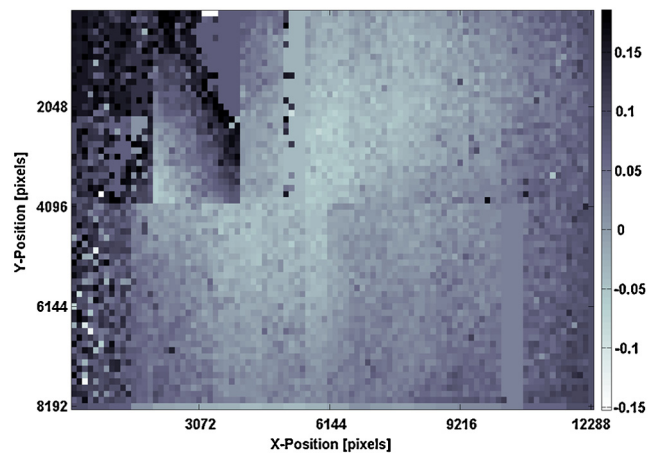


**Fig. 17** Map of the impact to the magnitude limit of observations due to the spot size variation across the focal plane. The pixel gray scale is in units of relative magnitude. (White pixels indicate no data.) The magnitude limit is computed from a model of the telescope system performance, which is a function of parameters including the telescope aperture size and focal ratio, the noise characteristics of the imager, and the PSF size. The measured PSF that is observed at each location on the focal plane (Fig. 16) is provided as input to the telescope model, producing a map of the expected magnitude limit across the focal surface. The spatial variation in PSF performance that is observed in Fig. 16 results in the estimated variation in magnitude limit shown in this figure.

## 6 Applicability of Methodology to Other Telescope Systems

The methodology for our alignment techniques can be applied to other potential three mirror telescopes, particularly for wide-field survey systems. Measurement of the full field aberration pattern in a wide-field system has been discussed for the case of wide-field Cassegrain telescopes,<sup>1</sup> where

the shape and orientation of the defocused stars provide information on the off-axis astigmatism. Since the SST does not have a dedicated wavefront sensor, we rely on measurements of the image aberrations using the DONUT algorithm. A telescope with a dedicated wavefront sensor could measure the system aberrations using a different process but would similarly need to be cognizant of aberration patterns across the full field-of-view.

Once the system aberrations are measured, the procedure to correct for the existing aberrations would depend on the optical design and the degrees of freedom available. The available degrees of freedom for the fine focus and alignment at the SST are bulk motions of the tertiary and secondary mirrors; tip, tilt, decenter, and piston along the optical axis. A different telescope with adjustment capability at the focal plane may apply corrections to the focal plane tip, tilt, or translation, whereas the SST applies position adjustments solely with the tertiary and secondary mirrors. Some systems will have the capability to deform the mirror shape and compensate for higher order terms. In principle, the techniques in use at the SST to measure the optical aberrations can be used in those systems. The difference would be in the corrective mirror motions applied.

## 7 Conclusion

This paper describes the successful program to achieve focus and alignment of the SST, a three-mirror Mersenne-Schmidt type telescope. The design and construction of the SST is unique, without precedent for the alignment methodology. There is no wavefront sensor or other dedicated test instrumentation available as a result of the camera installation at the telescope's prime focus. The degrees of freedom under our control for the purpose of alignment are tip, tilt, and decenter of the tertiary and secondary mirrors. The mirrors are moved as a solid body without application of mirror deformations.

Our methods for focus and alignment include analysis of out-of-focus images to estimate the image aberrations across the focal plane using a modified version of the software package DONUT.<sup>9</sup> The translation from image aberrations to mirror corrections was determined with reference to the Zemax sensitivity analysis of the relationship between mirror position and image aberrations. The focus and alignment program includes determining the corrections needed as a function of elevation to maintain performance from zenith to horizon pointing. We also construct a model to describe the correction to tertiary piston (focus) to maintain performance as the temperature changes, which is based on a year of empirical data.

Our methodology for focus and alignment of the SST has achieved a spot size of 28  $\mu\text{m}$  rms diameter during optimal seeing conditions, which compares favorably with the 28  $\mu\text{m}$  prediction of the pixilated spot size based on the Zemax model of the as-built optical system. We maintain nightly focus and alignment performance versus temperature and elevation to remain within <0.64 magnitudes performance impact (after correcting for airmass) for 90% of the time.

## Acknowledgments

This work is sponsored by the Defense Advanced Research Projects Agency under Air Force Contract #FA8721-05-C-0002. Opinions, interpretations, conclusions and recom-

mendations are those of the author and are not necessarily endorsed by the United States government.

## References

1. B. McLeod, "Collimation of fast wide-field telescopes," *Publ. Astron. Soc. Pac.* **108**(720), 217–219 (1996).
2. L. Noethe and S. Guisard, "Analytic expressions for field astigmatism in decentered two mirror telescopes and application to the collimation of the ESO VLT," *Astron. Astrophys. Suppl. Ser.* **144**(1), 157–167 (2000).
3. D. L. Terret and W. J. Sutherland, "The interaction between pointing and active optics on the VISTA telescope," *Proc. SPIE* **7740**, 77403A (2010).
4. A. Rakich et al., "Use of field aberrations in the alignment of the Large Binocular Telescope optics," *Proc. SPIE* **7012**, 70121L (2008).
5. D. R. Blanco, "Near-perfect collimation of wide-field Cassegrain telescopes," *Publ. Astron. Soc. Pac.* **124**(911), 36–41 (2012).
6. K. P. Thompson, T. Schmid, and J. P. Rolland, "The misalignment induced aberrations of TMA telescopes," *Opt. Express* **16**(25), 20345–20353 (2008).
7. J. Sebag et al., "LSST Telescope alignment plan based on nodal aberration theory," *Publ. Astron. Soc. Pac.* **124**(914), 380–390 (2012).
8. P. L. Schechter and R. S. Levinson, "Generic misalignment aberration patterns in wide-field telescopes," *Publ. Astron. Soc. Pac.* **123**(905), 812–832 (2011).
9. A. Tokovinin and S. Heathcote, "DONUT: measuring optical aberrations from a single extrafocal image," *Publ. Astron. Soc. Pac.* **118**(846), 1165–1175 (2006).
10. C.-J. Kim and R. R. Shannon, "Catalog of Zernike polynomials," Chapter 4 in *Applied Optics and Optical Engineering*, Vol. 10, R. R. Shannon and J. C. Wyant, Eds., Academic Press, New York (1987).
11. M. Born and E. Wolfe, *Principles of Optics*, Pergamon Press, New York (1964).
12. R. J. Noll, "Zernike polynomials and atmospheric turbulence," *J. Opt. Soc. Am.* **66**(3), 207–211 (1976).
13. F. Roddier, "Wavefront sensing and the irradiance transport equation," *Appl. Opt.* **29**(10), 1402–1403 (1990).
14. B. J. Thelen et al., "Maximum a posteriori estimation of fixed aberrations, dynamic aberrations, and the object from phase-diverse speckle data," *J. Opt. Soc. Am. A* **16**(5), 1016–1025 (1999).
15. F. Roddier, *Adaptive Optics in Astronomy*, Cambridge University Press, Cambridge (1999).
16. D. F. Woods, "Tidally triggered star formation and selected works in optical instrumentation," PhD Thesis, Harvard University (2009).
17. D. F. Woods et al., "The Space Surveillance Telescope: focus and alignment of a three mirror telescope," in *Proceedings of the 2012 AMOS Technical Conference*, Maui Economic Development Board, Maui, Hawaii (2012).

**Deborah Freedman Woods** holds the position of technical staff at MIT Lincoln Laboratory in the Sensor Technology and System Applications Group. She works in optical system design and analysis on issues that range from the alignment of the 3.5 m Space Surveillance Telescope (SST) and the development of an SST science program to the advancement of the Lincoln Near-Earth Asteroid Research (LINEAR) program, where she serves as a co-principal investigator, to the development of wavefront sensor measurement techniques and sensor performance characterization. Her areas of expertise include electro-optical astronomical techniques, sensor system calibration, and performance optimization of large ground-based telescopes. She holds an AB in astrophysics from Princeton and a PhD in astronomy from Harvard, where she focused on optical instrumentation and on research in galaxy photometry and spectroscopy.

**Ronak Y. Shah** serves at MIT Lincoln Laboratory, in the Space Control Systems Group and Aerospace Division. He works as the co-principal investigator on the long-running Lincoln Near Earth Asteroid Research (LINEAR) program, a significant contributor to NASA's Near Earth Object Observations office. He has worked as an observational astronomer for nearly 20 years, using ground- and space-based instruments across the electromagnetic spectrum, concentrating on radio (including interferometry), infrared, optical, and x-ray. He has contributed or written refereed publications on a number of diverse subjects in astrophysics, including star formation, chemical evolution of the interstellar medium, gravitational lensing, and Milky Way structure and evolution. Since joining Lincoln Laboratory, he has contributed to both flight and ground missions serving the US Air Force's space situational awareness mission. He is currently one of the team scientists on the DARPA Space Surveillance

Telescope, a next generation prototype that greatly improves the US capability to survey objects in deep space.

**Julie A. Johnson** is an associate staff member of the Space Control Systems at MIT Lincoln Laboratory. She has been working on operations interfaces of space surveillance systems since 1978. Some of the systems she has worked on include GEODSS, ETS, MOSS and SST. She was the principal designer of the mission software for the MIT Optical Surveillance System and Space Surveillance Telescope. She received a Master of Science in physics from the New Mexico Institute of Mining and Technology in 1977 and a Bachelor of Arts in mathematics from the University of California at San Diego in 1974. She joined the laboratory in 1984.

**Eric C. Pearce** is an associate group leader of the Space Control Systems at MIT Lincoln Laboratory. He has over 20 years of experience in many different aspects of the space surveillance/space control mission area. He is the technical director and program manager of the DARPA 3.5 m Space Surveillance Telescope (SST) Program, which recently achieved First Light in February 2011. He received his Doctorate of Astrophysics from the New Mexico Institute of Mining and Technology in 1988. His area of study was the automation and remote operation of an optical telescope to search for extra-galactic supernovae. From 1988 to 1989, he held a post-doctoral position at the University of Chicago Yerkes Observatory, working on the Apache Point 3.5 m telescope project. In 1989 joined the Laboratory, initially working at the remote Experimental Test System (ETS) near Socorro, New Mexico.

**Richard L. Lambour** received his BS in physics from Clemson University in 1989 and his PhD in space physics and astronomy in 1994 from Rice University. He worked for two years at the Air Force Research Laboratory on terrestrial space weather forecasting science and algorithm development before joining MIT Lincoln Laboratory in 1996. At the laboratory, he has worked as a data analyst and electro-optic systems engineer for multiple space- and ground-based sensor programs covering ultraviolet through long-wave infrared wavelength regimes. He has served for the past eight years as the system engineering lead for the Space Surveillance Telescope program.

**Walter J. Faccenda** holds the position of technical staff at MIT Lincoln Laboratory in the Space Control Systems Group within the Aerospace Division. He is an optical test and systems engineer and has been a member of the DARPA/Space Surveillance Telescope effort since 2010. During his years at The MITRE Corporation, he was the lead engineer for the Deep STARE CCD Camera and Mount Control System upgrades for the Ground-based Electro-Optical Deep Space Surveillance (GEODSS) system, having also worked on ground-based space surveillance radar systems. Earlier he worked at Litton Itek Optical Systems, where he contributed to ground-based and space-based system development. He received his BS in astronomy from the University of Massachusetts at Amherst, MA, and an MS in the field of electro-optics from Northeastern University in Boston, MA.

**Alexander Szabo:** biography and photograph not available.